Structural basis for Ca^{2+} selectivity of a voltage-gated calcium channel

Lin Tang[1,2,*], **Tamer M. Gamal El-Din**[1,*], **Jian Payandeh**[1,3], **Gilbert Q. Martinez**[1], **Teresa M. Heard**[1], **Todd Scheuer**[1], **Ning Zheng**[1,2], and **William A. Catterall**[1]

[1]Department of Pharmacology, University of Washington, Seattle, WA, 98195, USA

[2]Howard Hughes Medical Institute, University of Washington, Seattle, WA, 98195, USA

Abstract

Voltage-gated calcium (Ca$_V$) channels catalyze rapid, highly selective influx of Ca^{2+} into cells despite 70-fold higher extracellular concentration of Na$^+$. How Ca$_V$ channels solve this fundamental biophysical problem remains unclear. Here we report physiological and crystallographic analyses of a calcium selectivity filter constructed in the homotetrameric bacterial Na$_V$ channel Na$_V$Ab. Our results reveal interactions of hydrated Ca^{2+} with two high-affinity Ca^{2+}-binding sites followed by a third lower-affinity site that would coordinate Ca^{2+} as it moves inward. At the selectivity filter entry, Site 1 is formed by four carboxyl side-chains, which play a critical role in determining Ca^{2+} selectivity. Four carboxyls plus four backbone carbonyls form Site 2, which is targeted by the blocking cations, Cd^{2+} and Mn^{2+}, with single occupancy. The lower-affinity Site 3 is formed by four backbone carbonyls alone, which mediate exit into the central cavity. This pore architecture suggests a conduction pathway involving transitions between two main states with one or two hydrated Ca^{2+} ions bound in the selectivity filter and supports a "knock-off" mechanism of ion permeation through a stepwise-binding process. The multi-ion selectivity filter of our Ca$_V$Ab model establishes a structural framework for understanding mechanisms of ion selectivity and conductance by vertebrate Ca$_V$ channels.

Correspondence and requests for materials should be addressed to N.Z. (nzheng@uw.edu) and W.A.C. (wcatt@uw.edu).
[3]Present address: Department of Structural Biology, Genentech Inc., South San Francisco, CA, 94080, USA
*These authors contributed equally to this work

Ca^{2+} ions flow through voltage-gated Ca^{2+} (Ca_V) channels at a rate of ~10^6 ions/s, yet Na^+ conductance is >500-fold lower[1]. Such high-fidelity, high-throughput Ca_V channel performance is important to regulate intracellular processes such as contraction, secretion, neurotransmission, and gene expression in many different cell types[2]. Because the extracellular concentration of Na^+ is 70-fold higher than Ca^{2+}, these essential biological functions require Ca_V channels to be highly selective for Ca^{2+} in preference to Na^+, even though Ca^{2+} and Na^+ have nearly identical diameter (~2 Å). Ion selectivity of Ca_V channels is proposed to result from high-affinity binding of Ca^{2+}, which prevents Na^+ permeation. Fast Ca^{2+} flux through Ca_V channels is thought to utilize a 'knock-off' mechanism in which electrostatic repulsion between Ca^{2+} ions within the selectivity filter overcomes tight binding of a single Ca^{2+} ion[1,3–8]. Most of these mechanisms require a multi-ion pore, yet extensive mutational analyses of ion selectivity and cation block of vertebrate Ca_V channels support a single high-affinity Ca^{2+} binding site[1,9–14].

Ca_V channels contain a single ion-selective pore in the center of four homologous domains[2]. The central pore is lined by the S5 and S6 transmembrane helices and the intervening "P-loop" from each domain in a four-fold pseudosymmetric arrangement. The four voltage-sensing modules composed of S1–S4 transmembrane helices are symmetrically arranged around the central pore. Ca_V channels are members of the voltage-gated ion channel superfamily and are closely related to voltage-gated Na^+ (Na_V) channels. The structures of three homotetrameric bacterial Na_V channels open the way to elucidating the structural basis for ion selectivity and conductance of vertebrate Na_V and Ca_V channels[15–17], which likely evolved from the bacterial NaChBac family and retained similar structures and functions (Supplementary Fig. 1)[18–20]. Interestingly, mutation of three amino acid residues in the selectivity filter of NaChBac is sufficient to confer Ca^{2+} selectivity[21]. We have introduced analogous mutations into the bacterial Na_V channel Na_VAb to create Ca_VAb and carried out electrophysiological and X-ray crystallographic analyses to determine the relative permeability of Ca^{2+} and define ion-binding sites in the selectivity filter. Our systematic analyses of Ca_VAb and intermediate derivatives provide structural and mechanistic insights into Ca^{2+} binding and ion permeation and suggest a conductance mechanism involving two energetically similar ion occupancy states with one or two hydrated Ca^{2+} ions bound.

Structure and function of Ca_VAb

Na_VAb channels have four identical pore motifs (^{175}TLESWSM^{181}) that form the ion selectivity filter[15]. The side chains of E177 form a high-field-strength site ($Site_{HFS}$) at the outer end of the filter, while two additional potential Na^+ coordination sites, $Site_{CEN}$ and $Site_{IN}$, are formed by the backbone carbonyls of L176 and T175[15]. To create Ca_VAb, E177, S178, and M181 were substituted with Asp, resulting in a mutant with the pore motif ^{175}TL<u>DD</u>WS<u>D</u>^{181} (underlined letters indicate mutated residues). Ca_VAb was expressed in *Trichopulsia ni* cells (Hi5) and analyzed by whole-cell voltage clamp to determine its ion selectivity. In contrast to Na_VAb, which does not conduct extracellular Ca^{2+} ions but carries outward Na^+ current (Fig. 1a, b), Ca_VAb conducts inward Ca^{2+} current in a voltage-dependent manner (Fig. 1c, d). Complete titration curves for Ca^{2+} in the presence of Ba^{2+} as the balancing divalent cation (see Methods) revealed inhibition of Ba^{2+} current by low concentrations of Ca^{2+} followed by increases in Ca^{2+} current at higher Ca^{2+}

concentrations (Fig. 1e). These results demonstrate the anomalous mole fraction effect characteristic of vertebrate Ca_V channels. Comparable experiments with Na^+ as the balancing cation were not possible because of the instability of the Hi5 cells in solutions with low divalent cation concentrations. The reversal potential for Ca^{2+} current under bi-ionic conditions closely follows the expectation for a highly Ca^{2+}-selective conductance (30.6 ± 2.3 mV/decade, Fig. 1f; Supplementary Fig. 2), and Ca_VAb selects Ca^{2+} 382-fold over Na^+ under our standard recording conditions, yielding >10,000-fold $P_{Ca}:P_{Na}$ range for these constructs (Fig. 1g). Intermediate Ca_VAb derivatives with single and double Asp substitutions had progressive increases in Ca^{2+} selectivity (Fig. 1g; Supplementary Fig. 2), as observed for NaChBac[21]. The [175]TL$\underline{DD}$WS$\underline{N}$[181] mutant has an Asn residue in place of the final Asp, as observed in one domain of mammalian Ca_V channels (Supplementary Fig. 1), and it still favors Ca^{2+} over Na^+ by more than 100-fold (Fig. 1g).

We have crystallized and determined the structure of Ca_VAb and its derivatives by molecular replacement using the Na_VAb structure (PDB code 3RVY) as the search template (Supplementary Table 1). The overall structure of Ca_VAb is very similar to that of Na_VAb, with an RMSD of 0.4 Å (Fig. 1h). However, the electrostatic potential at the outer entry to the selectivity filter is more negative for Ca_VAb than for Na_VAb (Supplementary Fig. 3). The three negatively charged Asp residues introduced at the selectivity filter of Ca_VAb create a wide, short, electronegatively lined pore (6 Å diameter, 10 Å length) with no significant alteration in backbone structure with respect to Na_VAb (Fig. 1i, j, Supplementary Fig. 4). Thus, Ca^{2+} selectivity of Ca_VAb is mainly determined by the side chains of the amino acids at the selectivity filter.

Ca^{2+}-binding sites in the permeation pathway

The 3.2 Å resolution structure of the mutant [175]TL$\underline{DD}$WS$\underline{N}$[181] in the presence of 10 mM Ca^{2+} reveals electron densities in the selectivity filter consistent with three Ca^{2+} ions aligned on the central axis (Fig. 2a). In the outer vestibule leading to the selectivity filter, there are two additional less-intense on-axis peaks associated with weaker surrounding densities. To confirm the identity of the bound ions, we collected X-ray diffraction data at 1.75 Å wavelength and calculated the F^+_{ca}-F^-_{ca} anomalous difference map. Two strong peaks followed by a weaker peak on the intracellular side were found in the selectivity filter along the ion-conduction pathway, verifying three binding sites for Ca^{2+} (Fig. 2b). We name these Site 1, Site 2, and Site 3 from the extracellular to the intracellular side.

The Ca^{2+} ion at Site 1 is predominantly coordinated by the carboxyl groups of D178 (Site$_{EX}$ in Na_VAb), which define a plane at the selectivity filter entrance on the extracellular side of the bound Ca^{2+} ion (Fig. 2b). The distance between the carboxyl oxygen and Ca^{2+} is about 4.0 Å. This distance suggests that the ion binds at this site in a hydrated form because the ionic diameter of Ca^{2+} is 2.28 Å, too small to interact with the carboxylate anions directly but appropriate for interaction through bound water molecules. Further into the pore, the four acidic side chains of D177 (Site$_{HFS}$ in Na_VAb) are located along the wall of the selectivity filter rather than projecting into the lumen, thereby also allowing the binding of a fully hydrated Ca^{2+} ion (Fig. 2b). Different from Site 1, this central Ca^{2+} binding site (Site 2) is surrounded by a box of 4 carboxylate oxygen atoms from D177 above and 4 backbone

carbonyl oxygen atoms from L176 below (Site$_{CEN}$ in Na$_V$Ab), with oxygen-Ca^{2+} distances of 4.5 Å and 4.2 Å, respectively (Fig. 2b). At the intracellular side of the pore, the third Ca^{2+} binding site (Site 3) is composed of one plane of four carbonyls from T175 (Site$_{IN}$ in Na$_V$Ab), which point inward to the lumen (Fig. 2b). Here the Ca^{2+} ion lies nearly on the same plane as T175 carbonyls. The chemical environment of Site 3 hints at a lower affinity, consistent with its role in exit of Ca^{2+} from the selectivity filter into the central cavity. Throughout the selectivity filter, the oxygen-Ca^{2+} coordination distances are in the range of 4.0 – 5.0 Å, suggesting that the bound Ca^{2+} ion is continuously stabilized in a fully hydrated state when it passes through the pore. We observed diffuse electron density and in favorable cases discrete water molecules surrounding the bound Ca^{2+}, consistent with the presence of an inner shell of bound waters of hydration (Supplementary Fig. 5).

Although the anomalous difference map did not resolve clear peaks at the outer vestibule beyond the selectivity filter, we interpret the two on-axis 2F$_o$-F$_c$ densities above the three Ca^{2+} sites as two additional Ca^{2+} ions poised to enter the pore (Fig. 2a). This assignment is supported by the surrounding eight islets of density, which likely represent eight stabilized water molecules. Just as at Site 2 in the selectivity filter, these eight water molecules appear to serve as a square antiprism cage coordinating a hydrated Ca^{2+} ion at the center (Fig. 2a). The second Ca^{2+} ion located at the bottom of this cage is ~4.5 Å away from the four carboxyl oxygen atoms of D178, suggesting that part of its second hydration shell is replaced by D178 before the ion enters the selectivity filter. The selectivity filter, therefore, appears to select Ca^{2+} at its mouth by recognizing the Ca^{2+}-hydration complex and conduct Ca^{2+} by fitting the Ca^{2+}-hydration complex into the pore. Because Ca^{2+} is more electropositive than Na$^+$, it should bind more tightly in the ion selectivity filter of Ca$_V$Ab, providing a mechanistic basis for the block of Na$^+$ permeation by Ca^{2+} at low Ca^{2+} concentration and preferential permeation of Ca^{2+} at higher Ca^{2+} concentration (Supplementary Discussion).

Functional roles of key selectivity filter residues

Measurements of bi-ionic reversal potentials revealed that the relative permeability of different Ca$_V$Ab intermediate constructs for Ca^{2+} follows the order of CavAb (^{175}TL**DD**WS**D**^{181}) > ^{175}TL**DD**WS**N**^{181} > ^{175}TLE**D**WS**D**^{181} > ^{175}TLE**D**WSM^{181} > Na$_V$Ab (^{175}TLESWSM^{181}) > ^{175}TL**D**SWSM^{181} (Fig. 1g; Supplementary Fig. 2). A comparison of the Ca^{2+} selectivity ratios between ^{175}TLE**D**WSM^{181} and ^{175}TLESWSM^{181} (Na$_V$Ab) shows that substitution of S178 with Asp is sufficient to convert the selectivity from Na$^+$ to Ca^{2+} with >100-fold change in P$_{Ca}$:P$_{Na}$ (Fig. 1g). Placement of the Asp carboxyl side chain at this position allows formation of the first hydrated Ca^{2+} binding site in the selectivity filter (Fig. 2c; Supplementary Fig. 6). By contrast, S178 in Na$_V$Ab binds Ca^{2+} directly by displacing its hydration shell, which blocks conductance of both Na$^+$ and Ca^{2+} (Fig. 2d). Therefore, formation of Site 1 for binding hydrated Ca^{2+} is both necessary and sufficient for conferring Ca^{2+} selectivity over Na$^+$ to Na$_V$Ab.

The Ca^{2+} selectivity ratio of Ca$_V$Ab (^{175}TL**DD**WS**D**^{181}) is 5.5-fold higher than ^{175}TLE**D**WS**D**^{181} (Fig. 1g). This functional difference reflects a role of Site 2 in adjusting Ca^{2+} selectivity. Different from the side chains of D177 in Ca$_V$Ab

(^{175}TL$\underline{DD}$WS$\underline{D}^{181}$), which interact with the Ca^{2+} ion (Fig. 2e), the carboxyl group of E177 in ^{175}TLE$\underline{D}$WS$\underline{D}^{181}$ swings away from the selectivity filter and forms a hydrogen bond with D181 and the main-chain nitrogen atoms of S180 (Fig. 2f, Supplementary Fig. 7). Site 2 in ^{175}TLE$\underline{D}$WS$\underline{D}^{181}$, therefore, is exclusively formed by the four carbonyl oxygen atoms of L176, which conceivably leads to a lower Ca^{2+} binding affinity and a decreased Ca^{2+} selectivity. This comparison highlights both the importance of Site 2 in supporting high Ca^{2+} selectivity and the critical role of the backbone carbonyl groups of L176 in constructing this ion-binding site.

Distinct from D177 and D178, the N181 residue of ^{175}TL$\underline{DD}$WS$\underline{N}^{181}$ lies outside the ion-conducting pore and is not directly involved in Ca^{2+} ion coordination. In close proximity to the carboxyl groups of D178, which form a ring that lines the perimeter of the pore entryway, the side chain of N181 embraces the perimeter of the D178 ring by donating a hydrogen bond to its side chain carboxyls (Fig. 3a). Such a structural arrangement is also found in Ca$_V$Ab (^{175}TL$\underline{DD}$WS$\underline{D}^{181}$) (Fig. 3b), although the more electronegative environment created by the extra negatively charge residue, D181, likely attracts Ca^{2+} more strongly and confers a 4- to 5-fold higher degree of Ca^{2+} selectivity to Ca$_V$Ab (^{175}TL$\underline{DD}$WS$\underline{D}^{181}$) in comparison to ^{175}TL$\underline{DD}$WS$\underline{N}^{181}$ (Fig. 1g and Supplementary Fig. 3).

^{175}TL$\underline{DD}$WSM^{181}, which has the hydrophobic residue M181 packed next to the D178 ring, is the only Ca$_V$Ab intermediate that does not conduct Ca^{2+} (Supplementary Fig. 2). The crystal structure of this mutant reveals a blocking Ca^{2+} ion tightly bound at Site 1 in a dehydrated state with an oxygen-ion distance of 2.3 Å (Fig. 3c). Superposition analysis shows few structural differences between ^{175}TL$\underline{DD}$WSM^{181} and ^{175}TL$\underline{DD}$WS$\underline{N}^{181}$, except for the side chain of D178, which is fixed by N181 in ^{175}TL$\underline{DD}$WS$\underline{N}$ but unconstrained in ^{175}TL$\underline{DD}$WSM^{181} (Fig. 3a, c). This comparison indicates that N181 in ^{175}TL$\underline{DD}$WS$\underline{N}^{181}$ and D181 in Ca$_V$Ab play a critical role in engaging D178 and allowing the reversible binding of the Ca^{2+}-H_2O hydration complex for active Ca^{2+} conductance. Although the subtle difference in Ca^{2+} selectivity between ^{175}TLE$\underline{D}$WS$\underline{D}^{181}$ and ^{175}TLE$\underline{D}$WSM^{181} seems to argue against this conclusion (Fig. 1g), E177 in ^{175}TLE$\underline{D}$WSM^{181} actually plays a structural role equivalent to that of N181 in ^{175}TL$\underline{DD}$WS$\underline{N}^{181}$ — by pointing away from the selectivity filter lumen, E177 forms a carboxylate-carboxylate pair with D178 and holds it in a conduction-competent position (Fig. 3d, Supplementary Fig. 8).

Block of Na$_V$Ab and Ca$_V$Ab channels by divalent cations

Cd^{2+}, Mn^{2+} and other inorganic cations are effective blockers of Ca$_V$ channels[1]. Block of Ca^{2+} conductance of Ca$_V$Ab by Cd^{2+} and Mn^{2+} gives K_i values of 1.78 μM for Cd^{2+} and 526 μM for Mn^{2+} (Fig. 3e, f, blue). Cd^{2+} has lower affinity and Mn^{2+} has higher affinity for block of ^{175}TL$\underline{DD}$WS$\underline{N}^{181}$ (Fig. 3e, f, red). Crystals with bound Cd^{2+} and Mn^{2+} were obtained by soaking Ca$_V$Ab crystals in a cryo-solution containing these heavy metal ions, and the anomalous difference map was calculated from a dataset collected at 1.75Å wavelength. The structures show that both Cd^{2+} and Mn^{2+} bind in the selectivity filter at the central site (Site 2), which is coordinated by the side chains of the four D177 residues and the carbonyl groups of L176 (Fig. 3g, h). Locked at this site, these blocking ions would inhibit the Ca^{2+} current by competitively binding to the high affinity site required for Ca^{2+}

permeation. Another important common feature of the two blocking complexes of Ca_VAb is the block of permeation by binding of a single divalent cation within the selectivity filter, which supports the hypothesis that at least two divalent cation binding sites must be located close enough to induce repulsive interactions and allow divalent cation conductance by a knock-off mechanism. Because they are smaller than Ca^{2+}, the bound Cd^{2+} (d=2.18 Å) and Mn^{2+} (d=1.94 Å) must interact with the selectivity filter through bound waters of hydration, and electron density consistent with bound waters of hydration is observed in our structures (Supplementary Fig. 5).

Ion binding at the Ca^{2+} selectivity filter

To assess the properties of the three Ca^{2+} binding sites in the selectivity filter of [175]TL D D WS N[181], we titrated the concentration of Ca^{2+} in the cryo-solution and calculated the anomalous difference maps. At low Ca^{2+} concentration, two strong peaks of approximately equal intensity are found at Site 1 and Site 2 (Supplementary Fig. 9). As the Ca^{2+} concentration is raised, the electron density of Site 2 is substantially enhanced, but the peak intensity is reduced at Site 1 and remains low at Site 3 (Supplementary Fig. 9). These results imply that the central site has the highest affinity, whereas Site 3 is the weakest. It is likely that this titration pattern reflects independent binding of Ca^{2+} to Sites 1, 2, and 3 located in different individual molecules of Ca_VAb at low Ca^{2+} concentration, whereas increasing concentrations of Ca^{2+} saturate Site 2 in most or all individual Ca_VAb molecules and reduce or eliminate binding at Sites 1 and 3 by repulsion. Importantly, the two flanking sites have lower affinity than the central site, as proposed in the "stepwise binding model" of Ca_V channel permeation[7]. In this model, the presence of flanking sites of intermediate affinity facilitates the movement of Ca^{2+} into and out of a central high-affinity site, which can result in high ion conductance, even in the limiting case where there is no repulsion between bound ions.

Consistent with a high binding affinity, Ca^{2+} binds at Site 2 with its first hydration shell waters coordinated with eight oxygen atoms from the channel (Fig. 2b, Supplementary Fig. 5). In contrast, Ca^{2+} at Site 1 is mainly stabilized by one plane of four carboxyl groups from D178. The distance between the Ca^{2+} ion at Site 1 and the carboxyl group of D177 at Site 2 is about 5.5Å –6Å. As the Ca^{2+} ion moves inward, this distance will be reduced enough for D177 to form a stable coordination with the moving Ca^{2+} ion. This spatial configuration suggests that the two sites are separated by a low energy barrier. The differences of negative charge between D178 and the carbonyls of T175 and the differences in the geometry of their interactions with Ca^{2+} provide a plausible explanation for the higher Ca^{2+} binding affinity at Site 1 than Site 3.

Ion permeation mechanism

The three Ca^{2+}-binding sites in the selectivity filter of [176]L DD WS N[181] are separated by a distance of about 4.5 Å, which would result in substantial electrostatic repulsive interactions between bound ions. As in the case of the KcsA channel[22], it is energetically unfavorable for Ca^{2+} ions to occupy adjacent sites simultaneously. This leads directly to our hypothesis of two interchangeable functional states of the selectivity filter in the crystal structure (Fig. 4a,

b). In State 1, Ca^{2+} ions occupy Site 1 and Site 3. In State 2, a single Ca^{2+} ion occupies Site 2. These two states might be further coupled with one of the two Ca^{2+} ions at the outer vestibule ready to enter the pore (Fig. 4c). The transition between these two states occurs either when Ca^{2+} jumps from position 1 or 3 to position 2 or a third ion enters on one side of the filter, causing an ion to move into position 2. It is likely that our crystal structures reflect a mixed population of $Ca_V Ab$ molecules in which only Site 2 is occupied by Ca^{2+} plus $Ca_V Ab$ molecules in which Site 1 and/or Site 3 are occupied. Because of the high concentration of Ca^{2+} in the extracellular solution, Ca^{2+} will prefer to enter Site 1 and the weak binding of Ca^{2+} to Site 3 will force loss of Ca^{2+} into the low Ca^{2+} concentration in the cytosol. This generates a unidirectional flux of Ca^{2+} into the cell (Fig. 4c). The three-ion occupied state would be manifest only when the external Ca^{2+} concentration is increased enough that the flux reaches a limiting value[3]. The presence of the lower affinity Site 3 flanking the central cavity would further accelerate the flux of ions by allowing stepwise binding with relatively low chemical potential energy barriers[7]. The combination of ionic repulsion between Ca^{2+} ions bound at these sites and their stepwise change in binding affinity work together to allow rapid conductance in spite of the intrinsic high affinity for Ca^{2+} binding.

The mechanism underlying the dramatic difference in selectivity for Ca^{2+} over Na^+ in $Ca_V Ab$ versus $Na_V Ab$ is different from the mechanisms responsible for selectivity of K^+ over Na^+ and for Ca^{2+} block revealed by high-resolution structural studies of the NaK channel (Supplementary Discussion)[23–25]. Biophysical modeling of Ca^{2+} permeation in vertebrate Ca_V channels has led to multiple proposed mechanisms, most of which involve two or more Ca^{2+} binding sites, yet only a single high affinity site that is required for both permeation and Ca^{2+} block was identified by mutagenesis and physiological analyses[1]. Our results with $Ca_V Ab$ channels resolve this apparent discrepancy by showing that multiple Ca^{2+} binding sites are necessary for permeation, but only Site 2 binds divalent cations with sufficient affinity for block. Our results indicate that Ca^{2+} is conducted as a hydrated cation (Supplementary Discussion and Supplementary Fig. 5), consistent with the large estimated functional diameter of vertebrate Ca_V channels of $6Å$[26]. Detailed structure-function studies of vertebrate Ca_V channels show that mutations of the four residues equivalent to E177 have distinct effects on Ca^{2+} conductance and block, implying that domain-specific interactions with Ca^{2+} have evolved in vertebrate four-domain Ca_V channels [10,11,27–29]. Vertebrate Ca_V channels might share similar molecular mechanisms for Ca^{2+} permeation and selectivity despite their pseudosymmetric four-domain configuration.

METHODS

Protein expression and purification

The pFastBac-FLAG-$Na_V Ab$ (I217C) was used as the genetic background for $Ca_V Ab$ constructs was previously described[15,16]. $Ca_V Ab$ and its derivatives, [175]TL<u>DD</u>WS<u>N</u>[181], [175]TLE<u>D</u>WS<u>D</u>[181], [175]TLE<u>D</u>WSM[181], and [175]TL<u>D</u>SWSM[181] were generated via site-directed mutagenesis using QuickChange (Stratagene). Recombinant baculovirus were produced using the Bac-to-Bac system (Invitrogen), and *T. ni* insect cell were infected for large-scale protein purification. Cells were harvest 72 h post-infection and

re-suspended in 50 mM Tris-HCl pH=8.0, 200 mM NaCl (Buffer A) supplemented with protease inhibitors and DNase. After sonication, digitonin (EMD Biosciences) was added to 1% and solubilization was carried out for 1–2 h at 4°C. Clarified supernatant was then incubated with anti-Flag M2-agarose resin (Sigma) for 1–2 h at 4 °C with gentle mixing. Flag-resin was washed with ten column volumes of buffer B (buffer A supplemented with 0.12 % digitonin) and eluted with buffer B supplemented with 0.1 mg/ml Flag peptide. The eluent was concentrated and then passed over a Superdex 200 column (GE Healthcare) in 10 mM Tris-HCl pH=8.0, 100 mM NaCl and 0.12 % digitonin. The peak fractions were concentrated using a Vivaspin 30K centrifugal device.

Crystallization and data collection

$Ca_V Ab$ and its derivatives were concentrated to ~20mg ml^{-1} and reconstituted into DMPC:CHAPSO (Anatrace) bicelles according to standard protocols[30,31]. The protein-bicelle preparation and a well solution containing 1.8–2.0 M ammonium sulfate, 100 mM Na-citrate pH=5.0 was mixed with a 1:1 ratio and set up in a hanging-drop vapour-diffusion format. The Ca^{2+}- derivative crystals were obtained by soaking $Ca_V Ab$ and other mutant crystals in a cryo-protection solution (0.1M Na-acetate pH=5.0, 26% glucose and 2.0 M ammonium sulfate) containing the indicated concentrations of Ca^{2+} for 40–60 min at 4 °C. The Cd^{2+} and Mn^{2+} derivatives were obtained by soaking $Ca_V Ab$ in the presence of 100 mM Cd^{2+} or Mn^{2+}, respectively. Crystals were then plunged into liquid nitrogen and maintained at 100 K during all data collection procedures.

All anomalous diffraction datasets were collected at 1.75 Å with the same synchrotron radiation source (Advanced Light Source, BL8.2.1). To optimize the anomalous signal, the datasets were collected by using the "inverse beam strategy" with the wedge size of 5°.

Structure determination, refinement, and analyses

X-ray diffraction data were integrated and scaled with the HKL2000 package[32] and further processed with the CCP4 package[33]. The structure of $Ca_V Ab$ and its derivatives were solved by molecular replacement by using an individual subunit of the $Na_V Ab$ structure (PDB code 3RVY) as the search template. The datasets were processed in C2 space group and there are four molecules in one asymmetric unit. We choose the I222 space group to process the datasets for initial structural determination, but we found that the bound ions are slightly off-center with respect to the axis of the pore. Therefore, to better interpret the coordination of Ca^{2+}, Cd^{2+}, and Mn^{2+}, we solved the structures in the C2 space group. Crystallography and NMR System software [34] was used for refinement of coordinates and *B*-factors. Final models were obtained after several cycles of refinement with REFMAC[35] and PHENIX[36] and manual re-building using program COOT[37]. The geometries of the final structural models of $Ca_V Ab$ and its derivatives were verified using PROCHECK[38]. The divalent cations were identified by anomalous difference Fourier maps calculated using data collected at wavelengths of 1.75 Å for Ca^{2+}, Cd^{2+} and Mn^{2+}. Detailed crystallographic data and refinement statics for all the constructs are shown in Table S1. All structural figures were prepared with the PyMol software[39].

Electrophysiology

NavAb-WT expressed by infection of insect cells (High5) activates at very negative potentials V1/2 ~ −98 mV) and shows a strong, late use-dependent phase of slow inactivation. Mutation N49K shifts the activation curve ~75 mV to more positive potentials and abolishes the use-dependent inactivation[40]. All NavAb/CavAb constructs used were made on the background of N49K mutation and showed good expression, allowing measurement of ionic currents 24–48 h post-infection.

Whole-cell currents were recorded using an Axopatch 200 amplifier (Molecular Devices, Sunnyvale, CA) with glass micropipettes (2–5 MΩ). Capacitance was subtracted and 80–90% of series resistance was compensated using internal amplifier circuitry. For reversal potential measurements, the intracellular pipette solution contained (in mM): 100 NaF, 10 NaCl, 20 HEPES-Na, 10 EGTA, pH 7.4 (adjusted with NaOH, $[Na^+]_{Total} = 146$ mM). Extracellular solution contained in (mM) 10 $CaCl_2$, 140 NMDG-methanesulfonate, 20 HEPES, (pH 7.4, adjusted with $Ca(OH)_2$, $[Ca^{2+}]_{Total} = 12$ mM). For Ba^{2+} reversal potential measurements, $BaCl_2$ replaced $CaCl_2$. Current-voltage (I–V) relationships were recorded in response to steps to voltages ranging from −100 to +70 mV in 5 or 10 mV increments from a holding potential of −100 mV. Pulses were generated and currents were recorded using Pulse software controlling an Instrutech ITC18 interface (HEKA, Great Neck, NY). Data were analyzed using Igor Pro 6.2 (WaveMetrics, Lake Oswego, OR). Sample sizes were chosen to give SEM values of less than 10 % of peak values based on prior experimental experience.

Relative permeability values were calculated as described[41]. The permeability ratio was calculated as:

$$P_x/P_{Na} = a_{Na} \left[\exp\left(\frac{E_{rev}F}{RT}\right) \right] \left[\exp\left(\frac{E_{rev}F}{RT}\right) + 1 \right] / 4a_x$$

where F, R, T, and E*rev* are Faraday constant, gas constant, absolute temperature, and reversal potential, respectively. a_x, denotes the activity of the external divalent ion, x, (Ca^{2+} or Ba^{2+}) and a_{Na}, the activity of intracellular sodium. The calculated activity coefficients were $\gamma_{Ca} = 0.33$, $\gamma_{Ba} = 0.30$, $\gamma_{Na} = 0.74$. All potentials were corrected for the experimentally determined liquid junction potential.

For anomalous mole fraction and blocking experiments, the divalent (Ca^{2+}, Cd^{2+}, and Mn^{2+}) was diluted in 10 mM $BaCl_2$, 140 mM NMDG-methanesulfonate, and 10 mM HEPES and perfused for 2–3 min before recording a current-voltage curve. The peak value of the I–V curve was measured and normalized to the peak value without the divalent cation.

Supplementary Material

Refer to Web version on PubMed Central for supplementary material.

Acknowledgments

References

1. Sather WA, McCleskey EW. Permeation and selectivity in calcium channels. Annu Rev Physiol. 2003; 65:133–159. [PubMed: 12471162]

2. Catterall WA. Voltage-gated calcium channels. Cold Spring Harb Perspect Biol. 2011; 3:a003947. [PubMed: 21746798]

3. Almers W, McCleskey EW. Non-selective conductance in calcium channels of frog muscle: calcium selectivity in a single-file pore. J Physiol. 1984; 353:585–608. [PubMed: 6090646]

4. Almers W, McCleskey EW, Palade PT. A non-selective cation conductance in frog muscle membrane blocked by micromolar external calcium ions. J Physiol. 1984; 353:565–583. [PubMed: 6090645]

5. Hess P, Tsien RW. Mechanism of ion permeation through calcium channels. Nature. 1984; 309:453–456. [PubMed: 6328315]

6. Armstrong CM, Neyton J. Ion permeation through calcium channels. A one-site model. Ann N Y Acad Sci. 1991; 635:18–25. [PubMed: 1660235]

7. Dang TX, McCleskey EW. Ion channel selectivity through stepwise changes in binding affinity. J Gen Physiol. 1998; 111:185–193. [PubMed: 9450938]

8. Lopin KV, Obejero-Paz CA, Jones SW. Evaluation of a two-site, three-barrier model for permeation in $Ca(V)3.1$ (alpha1G) T-type calcium channels: Ca^{2+}, Ba^{2+}, Mg^{2+}, and Na^+ J Membr Biol. 2010; 235:131–143. [PubMed: 20512318]

9. Heinemann SH, Terlau H, Stuhmer W, Imoto K, Numa S. Calcium channel characteristics conferred on the sodium channel by single mutations. Nature. 1992; 356:441–443. [PubMed: 1313551]

10. Ellinor PT, Yang J, Sather WA, Zhang JF, Tsien RW. Ca^{2+} channel selectivity at a single locus for high-affinity Ca^{2+} interactions. Neuron. 1995; 15:1121–1132. [PubMed: 7576655]

11. Yang J, Ellinor PT, Sather WA, Zhang JF, Tsien RW. Molecular determinants of Ca^{2+} selectivity and ion permeation in L-type Ca^{2+} channels. Nature. 1993; 366:158–161. [PubMed: 8232554]

12. Kim MS, Morii T, Sun LX, Imoto K, Mori Y. Structural determinants of ion selectivity in brain calcium channel. FEBS Lett. 1993; 318:145–148. [PubMed: 8382625]

13. Cibulsky SM, Sather WA. The EEEE locus is the sole high-affinity Ca^{2+} binding structure in the pore of a voltage-gated Ca^{2+} channel: block by Ca^{2+} entering from the intracellular pore entrance. J Gen Physiol. 2000; 116:349–362. [PubMed: 10962013]

14. Cloues RK, Cibulsky SM, Sather WA. Ion interactions in the high-affinity binding locus of a voltage-gated Ca^{2+} channel. J Gen Physiol. 2000; 116:569–586. [PubMed: 11004206]

15. Payandeh J, Scheuer T, Zheng N, Catterall WA. The crystal structure of a voltage-gated sodium channel. Nature. 2011; 475:353–358. [PubMed: 21743477]

16. Payandeh J, Gamal El-Din TM, Scheuer T, Zheng N, Catterall WA. Crystal structure of a voltage-gated sodium channel in two potentially inactivated states. Nature. 2012; 486:135–139. [PubMed: 22678296]

17. Zhang X, et al. Crystal structure of an orthologue of the NaChBac voltage-gated sodium channel. Nature. 2012; 486:130–134. [PubMed: 22678295]

18. Ren D, et al. A prokaryotic voltage-gated sodium channel. Science. 2001; 294:2372–2375. [PubMed: 11743207]

19. Yu FH, Catterall WA. The VGL-chanome: a protein superfamily specialized for electrical signaling and ionic homeostasis. Sci STKE. 2004; 2004:re15. [PubMed: 15467096]

20. Koishi R, et al. A superfamily of voltage-gated sodium channels in bacteria. J Biol Chem. 2004; 279:9532–9538. [PubMed: 14665618]

21. Yue L, Navarro B, Ren D, Ramos A, Clapham DE. The cation selectivity filter of the bacterial sodium channel, NaChBac. J Gen Physiol. 2002; 120:845–853. [PubMed: 12451053]

22. Morais-Cabral JH, Zhou Y, MacKinnon R. Energetic optimization of ion conduction rate by the K$^+$ selectivity filter. Nature. 2001; 414:37–42. [PubMed: 11689935]

23. Alam A, Jiang Y. Structural analysis of ion selectivity in the NaK channel. Nat Struct Mol Biol. 2009; 16:35–41. [PubMed: 19098915]

24. Alam A, Shi N, Jiang Y. Structural insight into Ca^{2+} specificity in tetrameric cation channels. Proc Natl Acad Sci U S A. 2007; 104:15334–15339. [PubMed: 17878296]

25. Derebe MG, et al. Tuning the ion selectivity of tetrameric cation channels by changing the number of ion binding sites. Proc Natl Acad Sci U S A. 2011; 108:598–602. [PubMed: 21187421]

26. McCleskey EW, Almers W. The Ca channel in skeletal muscle is a large pore. Proc Natl Acad Sci U S A. 1985; 82:7149–7153. [PubMed: 2413461]

27. Chen XH, Tsien RW. Aspartate substitutions establish the concerted action of P-region glutamates in repeats I and III in forming the protonation site of L-type Ca^{2+} channels. J Biol Chem. 1997; 272:30002–30008. [PubMed: 9374474]

28. Cibulsky SM, Sather WA. Control of ion conduction in L-type Ca^{2+} channels by the concerted action of S5–6 regions. Biophys J. 2003; 84:1709–1719. [PubMed: 12609873]

29. Williamson AV, Sather WA. Nonglutamate pore residues in ion selection and conduction in voltage-gated Ca^{2+} channels. Biophys J. 1999; 77:2575–2589. [PubMed: 10545358]

30. Faham S, Bowie JU. Bicelle crystallization: a new method for crystallizing membrane proteins yields a monomeric bacteriorhodopsin structure. J Mol Biol. 2002; 316:1–6. [PubMed: 11829498]

31. Faham S, Boulting GL, Massey EA, Yohannan S, Yang D, Bowie JU. Crystallization of bacteriorhodopsin from bicelle formulations at room temperature. Protein Sci. 2005; 14:836–840. [PubMed: 15689517]

32. Otwinowski Z, Minor W. Processing of X-ray diffraction data collected in oscillation mode. Meth Enzymol. 1997; 276:307–326.

33. ccp4. The CCP4 suite: programs for protein crystallography. Acta crystallographica Section D, Biological crystallography. 1994; 50:760–763.

34. Brunger AT, Adams PD, Clore GM, DeLano WL, Gros P, Grosse-Kunstleve RW, Jiang JS, Kuszewski J, Nilges M, Pannu NS, Read RJ, Rice LM, Simonson T, Warren GL. Crystallography & NMR system: A new software suite for macromolecular structure determination. Acta crystallographica Section D, Biological Crystallography. 1998; 54:905–921.

35. Murshudov GN, Vagin AA, Dodson EJ. Refinement of macromolecular structures by the maximum-likelihood method. Acta crystallographica Section D, Biological crystallography. 1997; 53:240–255.

36. Adams PD, Afonine PV, Bunkoczi G, Chen VB, Davis IW, Echols N, Headd JJ, Hung LW, Kapral GJ, Grosse-Kunstleve RW, McCoy AJ, Moriarty NW, Oeffner R, Read RJ, Richardson DC, Richardson JS, Terwilliger TC, Zwart PH. PHENIX: a comprehensive Python-based system for macromolecular structure solution. Acta crystallographica Section D, Biological crystallography. 2010; 66:213–221.

37. Emsley P, Cowtan K. Coot: model-building tools for molecular graphics. Acta crystallographica Section D, Biological crystallography. 2004; 60:2126–2132.

38. Laskowski RA, Moss DS, Thornton JM. Main-chain bond lengths and bond angles in protein structures. J Mol Biol. 1993; 231:1049–1067. [PubMed: 8515464]

39. DeLano, WL. PyMOL molecular viewer(V12r3pre). 2002. (http://www.pymol.org)

40. Gamal El-Din TM, Martinez GQ, Payandeh J, Scheuer T, Catterall WA. A gating charge intereaaction required for late slow inactivation of the bacterial sodium channel NavAb. J Gen Physiol. 2013; 142:181–190. [PubMed: 23980192]

41. Yue L, Navarro B, Ren D, Ramos A, Clapham DE. The cation selectivity filter of the bacterial sodium channel, NaChBac. J Gen Physiol. 2002; 120:845–853. [PubMed: 12451053]
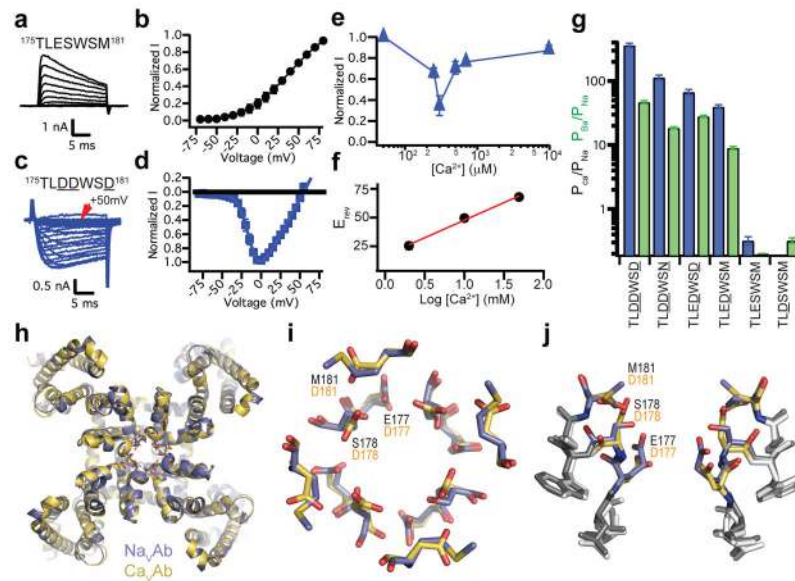
Figure 1. Structure and function of the Ca$_V$Ab channel

a, b, Outward Na$^+$ current conducted by Na$_V$Ab with 10 mM extracellular Ca^{2+} and 140 mM intracellular Na$^+$. Holding potential, -100 mV; 20-ms, 10-mV step depolarizations. **c, d,** Voltage-dependent conductance of inward Ca^{2+} current by Ca$_V$Ab under the same conditions. 20-ms, 5-mV step depolarizations. **e,** Biphasic anomalous mole fraction effect of increasing Ca^{2+} as indicated, with Ba^{2+} as the balancing divalent cation: 10 mM Ba^{2+} with 0 to 0.5 mM Ca^{2+}, 9.3 mM Ba^{2+} with 0.7 mM Ca^{2+}, and 0 mM Ba^{2+} with 10 mM Ca^{2+} (n = 4–10). **f.** Reversal potential (E$_{rev}$) versus Ca^{2+} concentration. **g,** Relative permeability of Ca$_V$Ab and its derivatives as measured from bi-ionic reversal potentials. P$_{Ca}$/P$_{Na}$, blue; P$_{Ba}$/P$_{Na}$, green (n=5–22). **h,** Cartoon representation of the overall structure of Ca$_V$Ab (yellow) superimposed with Na$_V$Ab (slate). **i, j,** Top and side views of the superimposed selectivity filters of Ca$_V$Ab (yellow) and Na$_V$Ab (slate) in stick representation. The three original NavAb residues (black) and substituted CavAb residues (orange) are indicated. Errors bars in **a**–**g** are standard error of the mean.
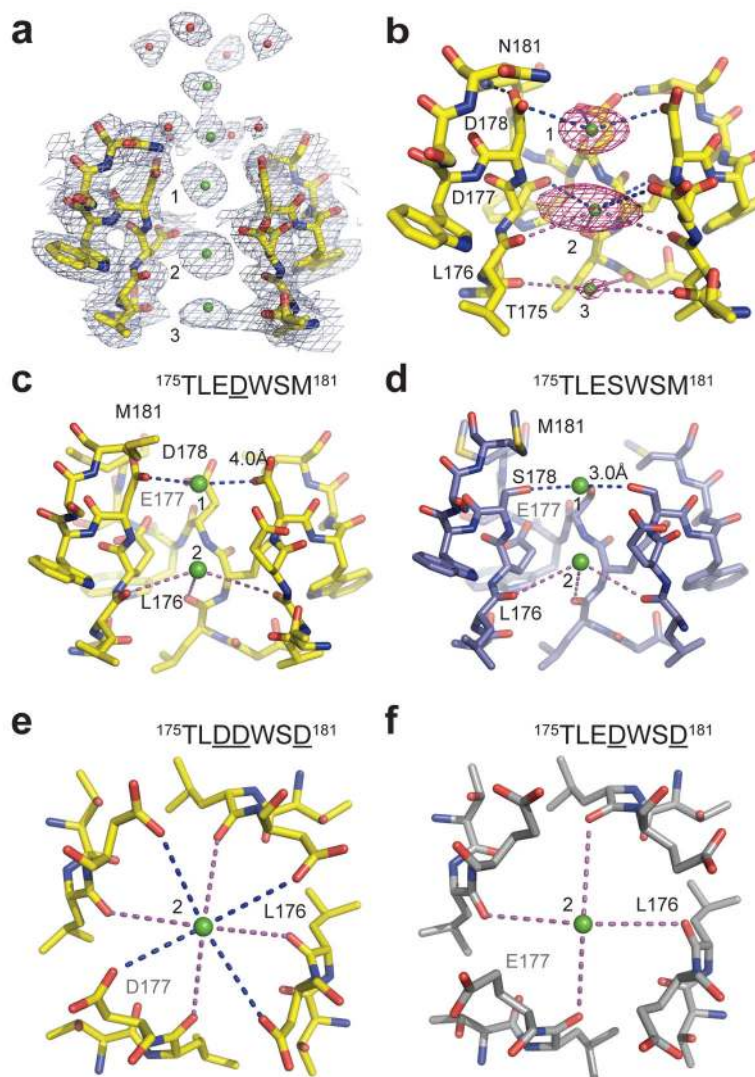
Figure 2. Ca^{2+} binding sites in and near the selectivity filter of Na$_V$Ab, Ca$_V$Ab, and their derivatives

a, Electron density at the selectivity filter of ^{175}TL<u>DD</u>WS<u>N</u>^{181} (also see Supplementary Fig. 4). The $2F_o-F_c$ electron density map (contoured at 2σ) of select residues in the selectivity filter with two diagonally opposed subunits shown in sticks, the Ca^{2+} ions along the ion pathway in green spheres and water molecules in red spheres. **b,** Densities at Ca^{2+} binding Site 1 and 2 from the anomalous difference Fourier map (3σ) calculated from the diffraction data of a ^{175}TL<u>DD</u>WS<u>N</u>^{181} mutant crystal soaked in the presence of 5 mM Ca^{2+} and collected at 1.75 Å wavelength. The distances between Ca^{2+} and oxygen atoms (dashed lines) are about 4.0 Å at Site 1 (blue lines), 4.4 Å at Site 2 (blue and magenta lines), and 5.0 Å (magenta line) at Site 3. For clarity, the subunit closest to the viewer is not shown. **c, d,** A comparison between ^{175}TLE<u>D</u>WSM^{181} and ^{175}TLESWSM^{181} (Na$_V$Ab) highlighting the importance of Site 1 for Ca^{2+} selectivity. **e, f,** A comparison between ^{175}TL<u>DD</u>WS<u>D</u>^{181} (Ca$_V$Ab) and ^{175}TLE<u>D</u>WS<u>D</u>^{181} highlighting the role of Site 2 in fine tuning Ca^{2+} selectivity. All structures were determined in the presence of 15 mM Ca^{2+}.
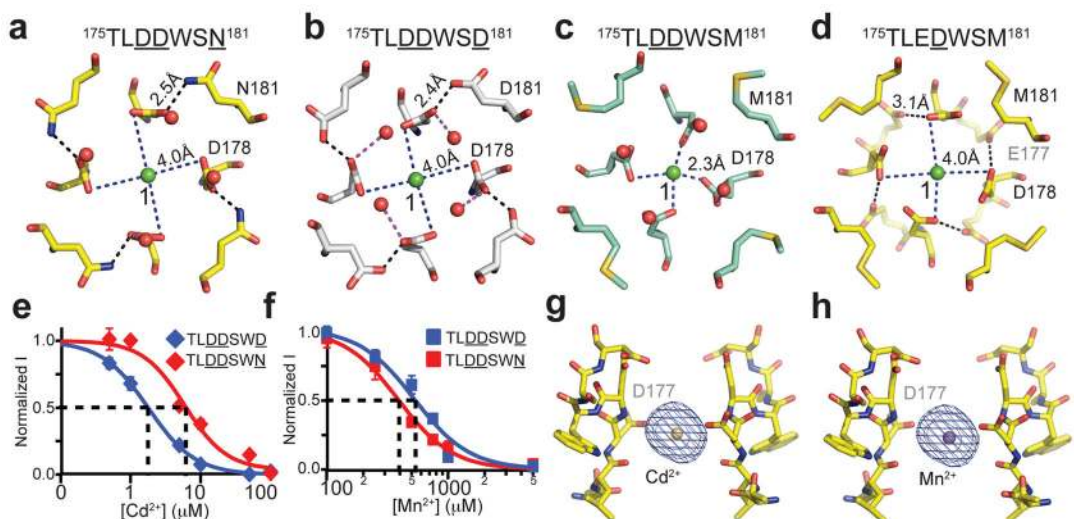
Figure 3. Ion binding and block of Ca$_V$Ab and its derivatives

a, b, Top view of Site 1 with a hydrated Ca^{2+} ion coordinated by D178 with the help of N181 and D181 in ^{175}TL$\underline{DD}$WS$\underline{N}$^{181} and ^{175}TL$\underline{DD}$WS$\underline{D}$^{181} (Ca$_V$Ab), respectively. **c,** Binding of a dehydrated Ca^{2+} ion at Site 1 in the nonconductive ^{175}TL$\underline{DD}$WSM^{181} mutant. **d,** Coordination of a hydrated Ca^{2+} ion at the Site 1 of the ^{175}TLE$\underline{D}$WSM^{181} mutant. Despite the absence of a polar residue at amino acid 181, E177 in ^{175}TLE$\underline{D}$WSM^{181} is able to hold D178 in place to allow the binding of a hydrated Ca^{2+} ion. **e, f,** Block of Ca^{2+} conductance by the indicated concentrations of Cd^{2+} and Mn^{2+}. ^{175}TL$\underline{DD}$WS$\underline{D}$^{181}: IC$_{50}$(Cd^{2+}), 1.7±0.04 μM; IC$_{50}$(Mn^{2+}, 526±22 μM. ^{175}TL$\underline{DD}$WS$\underline{N}$^{181}: IC$_{50}$(Cd^{2+}), 5.9±0.4 μM; IC$_{50}$(Mn^{2+}), 388±7 μM. **Error bars are standard error of the mean. g, h,** Side view of the Cd^{2+} and Mn^{2+} binding sites in the selectivity filter of Ca$_V$Ab. The anomalous difference Fourier map densities (blue mesh, contoured at 5σ) of the bound blocking ions are calculated using diffraction data collected at 1.75 Å wavelength. For clarity, the residues forms the selectivity filter of the closest subunit to the viewer is removed.
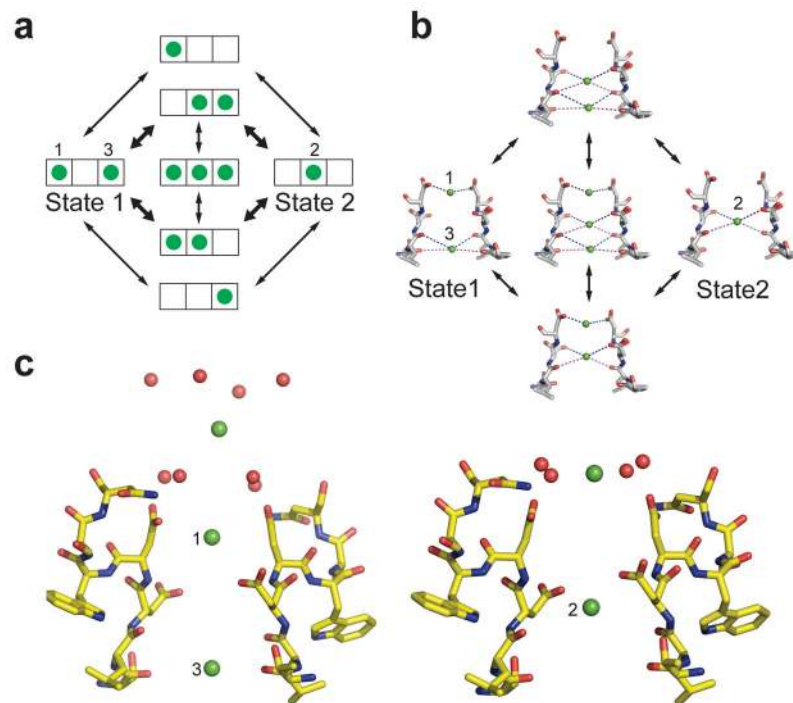
Figure 4. Catalytic cycle for Ca²⁺ conductance by Ca$_V$Ab

a, An ionic occupancy state diagram of Ca$_V$Ab showing two proposed low energy states and the potential transitions that connect them. Each state of the selectivity filter is represented by a three-box rectangle with Sites 1 – 3 going from left to right. Green circles represent Ca²⁺ ions. Note that transitions in the inner circle potentially lead to ion repulsion, which might facilitate conduction. These transitions in the inner circle are more probable than those in the outer circle, as denoted by the bold arrows. **b,** The structural basis of the ionic occupancy states depicted in the inner circle of the state diagram shown on the left. The clockwise cycle represents a path for inward flux of Ca²⁺ ions through the selectivity filter. **c,** Coupling of extracellular Ca²⁺ binding sites and the three sites within the selectivity filter in the two proposed ionic occupancy states. When two Ca²⁺ ions bind to position 1 and 3 in the filter, the entryway Ca²⁺ ion is placed furthest from the pore (left). When one Ca²⁺ ion binds to position 2 within the filter, the ion outside the filter is pulled closer to the pore (right).